THE ASTRONOMICAL JOURNAL, 121:727–739, 2001 February

THE INTERACTION BETWEEN THE INTERSTELLAR MEDIUM AND STAR FORMATION IN THE DWARF STARBURST GALAXY NGC 4214

FABIAN WALTER
Department of Astronomy, 105-24, California Institute of Technology, 1201 East California Boulevard, Pasadena, CA 91125
CHRISTOPHER L. TAYLOR
Five College Radio Astronomy Observatory, University of Massachusetts, Amherst, MA 01003
SUSANNE HÜTTEMEISTER
Radioastronomisches Institut der Universität Bonn, Auf dem Hügel 71, D-53121 Bonn, Germany
NICK SCOVILLE
Department of Astronomy, 105-24, California Institute of Technology, 1201 East California Boulevard, Pasadena, CA 91125
AND
VINCENT MCINTYRE
Australia Telescope National Facility, CSIRO, P.O. Box 76, Epping, NSW 1710, Australia
Received 2000 October 8; accepted 2000 November 3

ABSTRACT

We present the first interferometric study of the molecular gas in the metal-poor dwarf starburst galaxy NGC 4214. Our map of the ^{12}CO (1–0) emission, obtained at the Owens Valley Radio Observatory's millimeter array, reveals an unexpected structural wealth. We detected three regions of molecular emission in the northwest, southeast, and center of NGC 4214 that are in very different and distinct evolutionary stages (total molecular mass: $\sim 5.1 \times 10^6\ M_\odot$). These differences are apparent most dramatically when the CO morphologies are compared with optical ground-based and *Hubble Space Telescope* imaging: massive star formation has not started yet in the northwestern region; the well-known starburst in the center is the most evolved, while star formation in the southeastern complex has begun more recently. We derive a star formation efficiency of $\sim 8\%$ for the southeastern complex. Using high-resolution VLA observations of neutral hydrogen (H I) and our CO data, we generated a total gas column density map for NGC 4214 (H I + H_2). No clear correlation is seen between the peaks of H I, CO, and the sites of ongoing star formation. This emphasizes the irregular nature of dwarf galaxies. The H I and CO velocities agree well, as do the Hα velocities. In total, we cataloged 14 molecular clumps in NGC 4214. Our results from a virial mass analysis are compatible with a Galactic CO-to-H_2 conversion factor for NGC 4214 (lower than what is usually found in metal-poor dwarf galaxies).

Key words: galaxies: dwarf — galaxies: ISM

1. INTRODUCTION

Previous studies have shown that molecular gas is hard to study in dwarf galaxies, even in those known to be rich in neutral atomic gas (H I), such as dwarf irregulars (dIrr's) and blue compact dwarfs (BCDs). As carbon monoxide (CO) is the second most common molecular species after molecular hydrogen (H_2) and the one most easily observed in its cool, unshocked state, it is usually used as a tracer of molecular gas. Relatively few dwarf galaxies have been detected in CO, though many have been observed (see, e.g., Taylor, Kobulnicky, & Skillman 1998; Barone et al. 2000). Dwarf galaxies are set apart from other H I–rich galaxies by their low metallicity: Recent work suggested that the CO-to-H_2 conversion factor ("X") is dependent upon the metallicity of the gas, with the conversion factor increasing as metallicity decreases (Arimoto, Sofue, & Tsojimoto 1996; Wilson 1995; Verter & Hodge 1995; Rubio et al. 1991). Maloney & Black (1988) argued on theoretical grounds that at low metal abundances, the column density of CO will be lower and there will be less self-shielding from dissociating radiation. This will cause the size of the CO-emitting region to shrink while leaving the H_2 unaffected. Norman & Spaans (1997) predict that metallicities starting somewhere between 0.03 and 0.1 of the solar value are necessary before CO will be detectable. Observationally, Taylor et al. (1998) have found no dwarf galaxies with detectable CO emission at metallicities below ~ 0.15 solar. However, at present there are too few dwarfs with both metallicity measurements and CO observations to determine reliably whether there is indeed a cutoff, and where exactly it might take place.

For the few dwarfs that have been detected in CO, following up those single-dish detections with high spatial resolution interferometer data has proved enlightening. In some cases, the high resolutions of the interferometers allow the direct estimate of the total mass of resolved giant molecular clouds in nearby dwarf galaxies independent of the CO intensity and, from this, a first determination of the CO-to-H_2 conversion factor (e.g., Wilson 1995). A list of dwarf galaxies that have been observed with interferometers to date is compiled in Table 1. For example, Taylor et al. (1999) used the Plateau de Bure (PdB) interferometer to observe CO (1–0) and (2–1) in the poststarburst dwarf galaxy NGC 1569. They found that the conversion factor was 3 times higher than in two other dwarf galaxies of the same metallicity (NGC 6822 and IC 10), suggesting that metallicity is not the only influence upon the conversion factor. Motivated by this and other previous studies, we have observed another starburst dwarf galaxy, NGC 4214, at Owens Valley.

NGC 4214 is a nearby dwarf galaxy currently experiencing high levels of massive star formation. Table 2 summarizes some of the properties of NGC 4214. Combining

TABLE 1

INTERFEROMETRIC CO (1–0) STUDIES OF DWARF GALAXIES

Object	D (Mpc)	Telescope	Resolution (arcsec)	Lin. Res.[a] (pc)	Noise[b] (mJy beam^{-1})	Noise[b] (mK)	References
NGC 6822.....	0.49	OVRO	6.2 × 11.1	15 × 27	150	200	Wilson 1994
IC 10[c]	0.70	OVRO	6.6 × 7.5	~25	230	420	Wilson & Reid 1991
			5.5 × 9.5	20 × 33	150	260	Wilson 1995
NGC 205	0.83	BIMA	10.0 × 5.0	40 × 20	87	160	Young & Lo 1997
NGC 1569.....	2.2	PdB	4.5 × 3.9	~45	6	30	Taylor et al. 1999
NGC 5253.....	2.8	OVRO	14.9 × 11.4	202 × 155	200	200	Turner, Beck, & Hurt 1997
NGC 3077.....	3.2	OVRO	3.7 × 3.0	~50	24	200	Walter et al. 2001
M82	3.2	BIMA	2.3 × 2.6	~40	250	3800	Shen & Lo 1995
NGC 4214.....	4.1	OVRO	4.8 × 4.2	~90	33	150	This study
Henize 2-10.....	9.0	OVRO	6.5 × 5.5	~270	100	260	Kobulnicky & Skillman 1996
Mrk 190	17.0	OVRO	11.0 × 6.0	935 × 510	53	75	Li et al. 1994

[a] For small deviations from a circular beam, only the mean diameter is given.
[b] Noise assuming a channel width of 1 MHz (2.6 km s^{-1}).
[c] Two regions have been mapped in IC 10.

optical, near-IR, and UV data, Huchra et al. (1983) concluded it went through a burst of star formation a few times 10^7 yr ago. NGC 4214 has two main regions of star formation—a large complex of H II regions displaying a shell morphology in the galaxy center and a smaller southern complex formed mainly of compact knots (MacKenty et al. 2000). From age determinations of the H II regions and their spatial distribution, MacKenty et al. argue that some of the younger star formation has been triggered by the interaction of the older H II regions with the surrounding interstellar medium (ISM). At a distance of 4.1 Mpc (Leitherer et al. 1996), it is one of the closest star-bursting dwarf galaxies and thus an excellent target for a high-resolution study of the molecular ISM. Several groups have made single-dish CO observations of NGC 4214 (Tacconi & Young 1985; Thronson et al. 1988; Ohta et al. 1993; Becker et al. 1995; Taylor et al. 1998). While the existence of CO emission away from the center of NGC 4214 can be inferred from the single-dish data of Ohta et al. (who, however, fail to detect the central emission peak) and Taylor et al., no analysis of the distribution of the molecular emission and its relation to the major star-forming regions of the galaxy has been presented to date. Thronson et al. (1988) have also measured the dust mass in a region about 4′ in size using 160 μm data. The H I emission has been studied by Allsopp (1979) and McIntyre (1998), who find a large, extended H I disk and a complex velocity field in the center. Based on the disturbed inner velocity field, Allsopp (1979) argued that NGC 4214 is interacting with NGC 4190, a dIrr with a projected distance of 35 kpc.

In § 2, we describe our CO observations obtained with the Owens Valley Radio Observatory (OVRO). In § 3, we discuss the properties of the CO-emitting regions detected by the interferometer and compare them with high-resolution VLA H I imaging, as well as optical ground-based and *Hubble Space Telescope* (*HST*) imaging of NGC 4214. In § 4, we will discuss the conversion factor, the star formation efficiency, and implications on the star formation threshold as derived from our CO and H I data, as well as the interplay of the star formation regions on the surrounding ISM in NGC 4214. We summarize our results in § 5.

TABLE 2

PROPERTIES OF NGC 4214

Property	Value
R.A. (J2000.0)	$12^h15^m39^s.1$
Decl. (J2000.0)	36°19′39″
$V(\mathrm{sys})_{\mathrm{LSR}}$	300 km s^{-1}
Distance[a]	4.1 Mpc
1″	20 pc
$M_{\mathrm{H\,I}}$[b]	$1.0 \times 10^9\ M_\odot$
B_T[c], M_B[c]	10.2, −18.8
$12 + \log(\mathrm{O/H})$[d]	8.22
L_{FIR}[e]	$6.3 \times 10^8\ L_\odot$
Star formation rate[f]	$\sim 0.4\ M_\odot\ \mathrm{yr}^{-1}$

[a] Leitherer et al. 1996.
[b] Swaters 1999.
[c] De Vaucouleurs et al. 1991.
[d] Kobulnicky & Skillman 1995.
[e] Thronson et al. 1988.
[f] MacKenty et al. 2000.

2. OVRO OBSERVATIONS

2.1. *Observations and Data Reduction*

We observed NGC 4214 in the CO (1–0) transition, using the OVRO millimeter interferometer in mosaicking mode in C and L configurations. In total, 50 hr were spent on source. The observational details are listed in Table 3. Data were recorded using two correlator setups, resulting in velocity resolutions of 5 and 1.3 km s^{-1} (after on-line Hanning smoothing) with total bandwidths of 320 and 80 km s^{-1}, respectively. The absolute flux calibration was determined by observing 3C 273, 3C 345, and (in some observing periods) Neptune for approximately 20 minutes during each observing run. These calibrators and an additional noise source were used to derive the complex bandpass corrections. The quasar 1156+295, which is close to NGC 4214 in the sky, was used as a secondary amplitude and phase calibrator. During the program, its flux decreased from ~4.0 Jy (1999 September) to ~1.0 Jy (2000 June).

The data for each array were edited and calibrated separately with the MMA and MIRIAD packages. The *u-v* data were inspected and bad data points due to either interference or shadowing between telescopes were removed, after which the data were calibrated. We Fourier-transformed our C- and L-configuration observations separately for each pointing, to assess their quality; subse-

TABLE 3

SUMMARY OF THE OVRO OBSERVATIONS

A.

Parameter	C Configuration	L Configuration
Baselines	7–22 kλ (20–60 m)	6–44 kλ (15–115 m)
Tracks	1999 Sep 27–28, Oct 2; 2000 Jun 2–4	1999 Oct 10, Nov 9; 2000 Mar 27 Apr 11–12, Apr 29, May 6

B.

Parameter	Setup 1	Setup 2
Total bandwidths	124 MHz	31 MHz
No. of channels	62	62
Velocity resolution.....	5 km s^{-1}	1.3 km s^{-1}

C.

Parameter	Natural Weighting	Robust Weighting
Angular resolution.....	$6''.4 \times 5''.7$	$4''.8 \times 4''.2$
Linear resolution[a].....	131 × 117 pc	98 × 86
rms noise[b]	40 mJy beam^{-1} (100 mK)	47 mJy beam^{-1} (210 mK)

[a] Adopting a distance of 4.1 Mpc.

[b] Noise is given for a 1.3 km s^{-1} resolution channel.

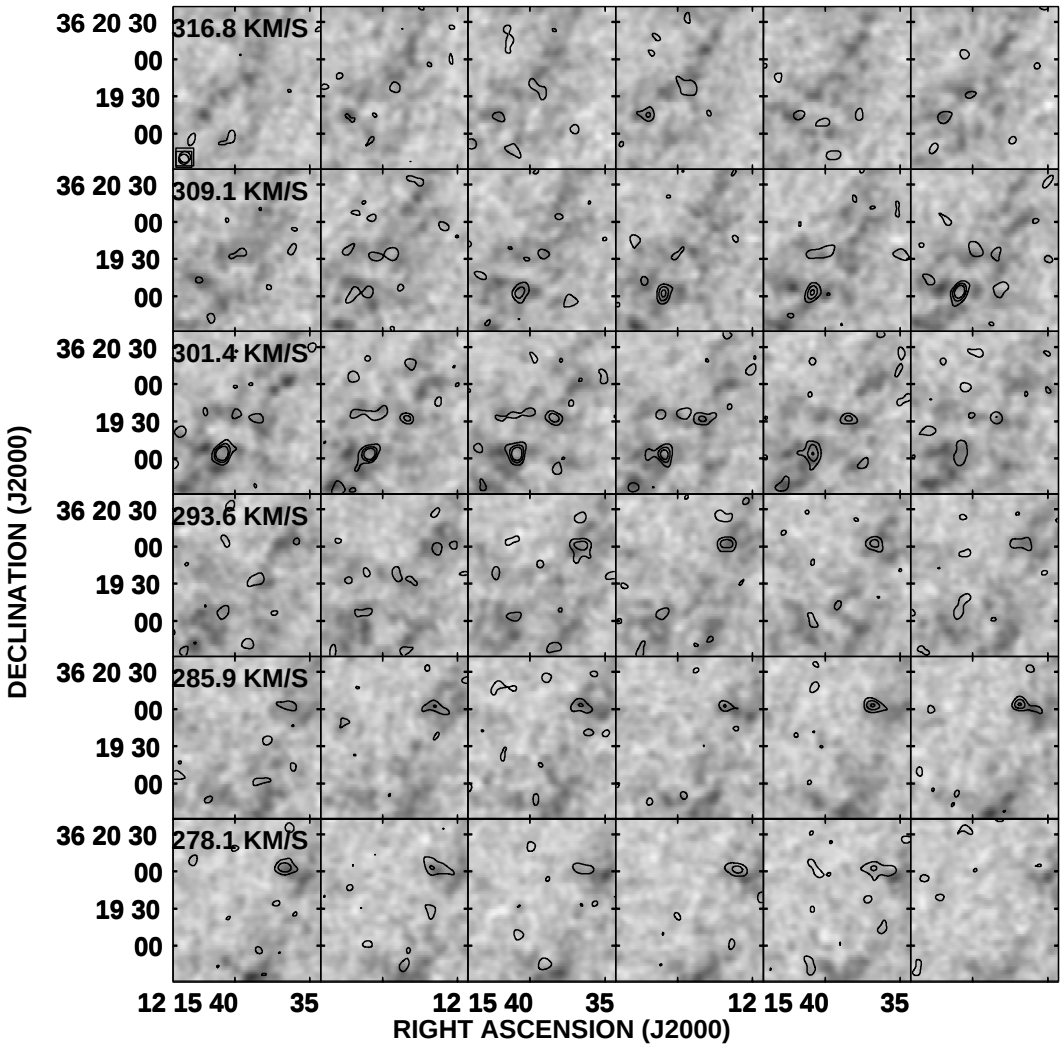

FIG. 1.—Cleaned channel maps of CO emission (contours convolved to 9″ resolution) superposed on the same channels of H I emission (*gray scale*). The contours show 2.5, 5, and 7.5 σ, where 1 σ = 40 mJy beam^{-1}. Channel separation is 1.3 km s^{-1}.

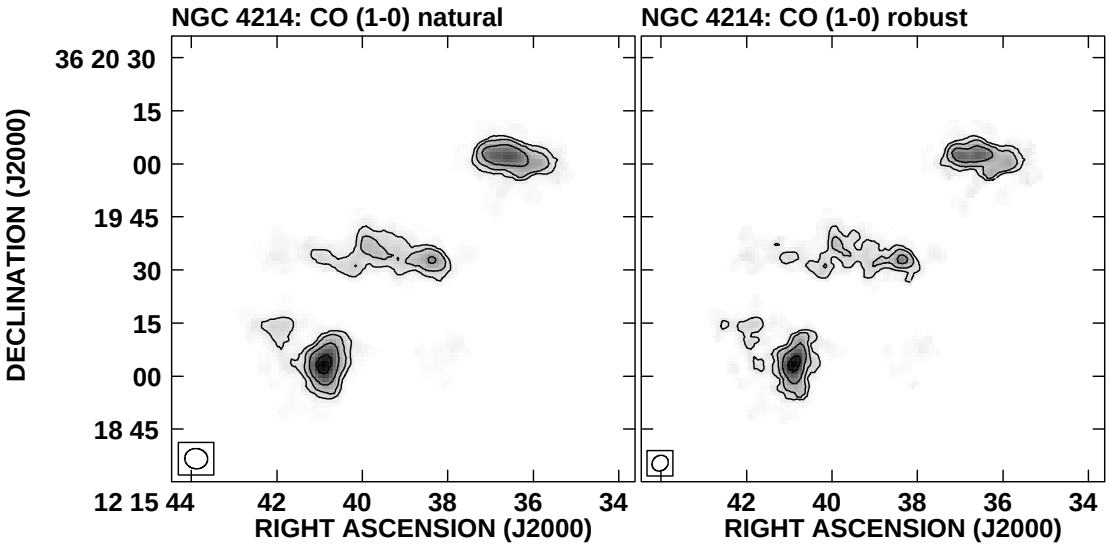

FIG. 2.—Integrated intensity maps of CO (1–0) emission in NGC 4214 (*gray scale and contours*). The left panel shows the naturally weighted map (6.″5 × 5.″7 [131 × 117 pc] resolution), and the right panel shows the robustly weighted map (4.″8 × 4.″2 [98 × 86 pc] resolution). The contours show 10%, 20%, 40%, and 80% of the peak intensity (natural: 5.0 Jy beam^{-1} km s^{-1}; robust: 3.9 Jy beam^{-1} km s^{-1}).

quently, we combined all data to form a single data set, which was used for mapping. The mosaicking and mapping was performed using the task MOSSDI in MIRIAD, i.e., a joint deconvolution of the entire mosaic was done to obtain the final data cubes. All the results presented in this paper are based on this combined data set.

We calculated two data cubes, one with natural weighting, leading to a resolution of 6.″4 × 5.″7, and another one with robust weighting (setting the robust parameter to zero; Briggs 1995) with a resolution of 4.″8 × 4.″2. The final rms noise in our 1.3 km s^{-1} wide channels was 40 mJy beam^{-1} (100 mK) and 47 mJy beam^{-1} (210 mK) for the naturally and robustly weighted cubes, respectively. We optimized the cleaning process by defining three clean boxes around the prominent emission regions. A summary of the observations can be found in Table 3. Channel maps of the data cube are presented as contours in Figure 1.

2.2. *Data Reduction*

We distinguished CO emission from the noise, using the following procedure: The cleaned 1.3 km s^{-1} data cube was smoothed to a spatial resolution of 9″ × 9″, and a 2 σ (80

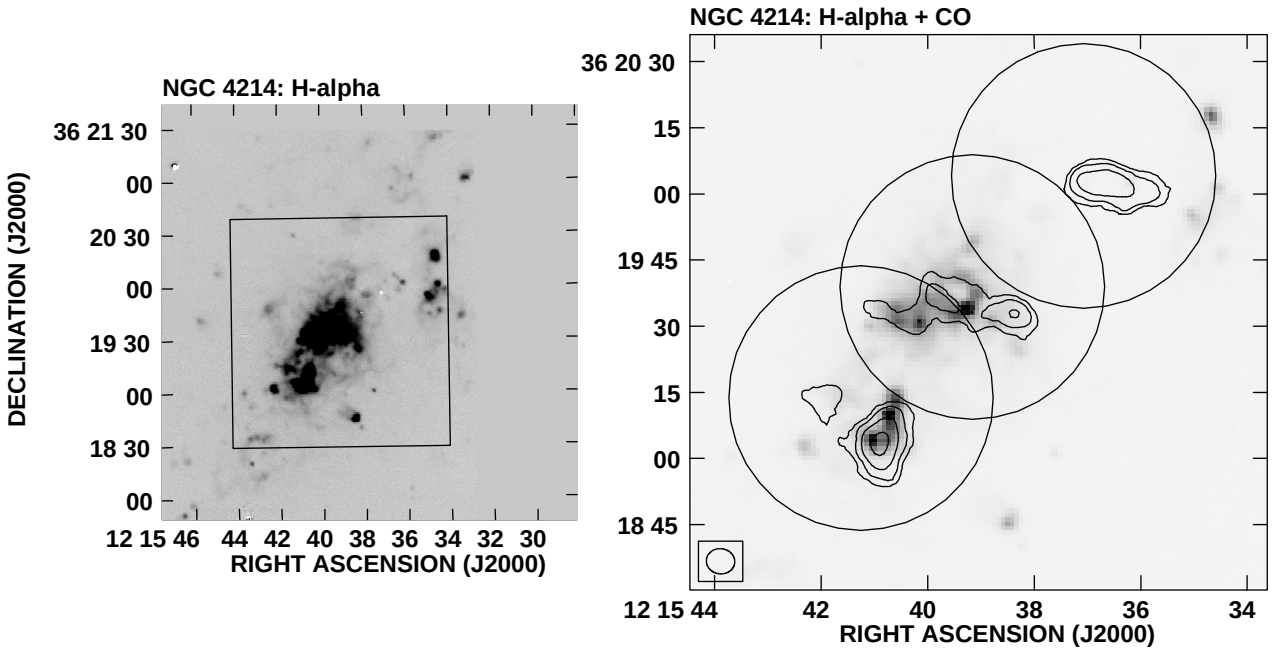

FIG. 3.—*Left:* Image of Hα + [N II] emission in NGC 4214, with the contrast set to show the low surface brightness features. The box indicates the region shown in the right panel. The gray scale has been chosen to bring out faint Hα filaments in addition to the bright H II regions. *Right:* Naturally weighted CO contours from Fig. 2 superposed on the Hα + [N II] emission. The large circles show the area covered in our CO mosaic. The gray scale is set lower to show the H II regions without saturation. Only a very faint H II region is visible at the position of the northwestern CO complex, while strong Hα emission is obvious at the positions of the central and southeastern complexes.

mJy beam^{-1}) blanking was applied to the output cube. The resulting cube was searched for CO emission by looking for surviving features, which were continuous in at least three consecutive channels. This gave a cube containing only the CO emission at a resolution of 9″. This cube was then applied as a mask to the original-resolution, naturally weighted cube to yield the final blanked data cube. The mask was also applied to the robustly weighted cube, and moment maps were made from the data of both weightings (Fig. 2).

The locations and sizes (FWHM) of the OVRO primary beams making up our mosaic are shown in Figure 3. While we cannot be certain to have detected all the CO emission in NGC 4214, we have probably mapped all the strong emission. Our first set of observations included only the center mosaic position, but in those data, we still detected both the northwestern and southeastern regions, even though they lay beyond the 40% power radius of the primary beam. Therefore, if there were any similar CO features just beyond the beam areas shown in Figure 3, we would have detected them.

It would be interesting to estimate the degree of missing flux due to the lack of short spacings in our interferometric map. This might give some indication of the amount and distribution of diffuse gas in and between the complexes. Unfortunately, there are no single-dish observations of the CO distribution in NGC 4214 that are suitable for such a determination. The single-dish beam is either very large (50″–55″), with a pointing center offset from the peak position of any complex, thus partially containing several complexes (Taylor et al. 1998; Thronson et al. 1988; Tacconi & Young 1985), or the observed region is not sufficiently extended and spatially disjunct (Ohta et al. 1993), or the observations were done in a different transition (Becker et al. 1995 for the central complex).

3. RESULTS

3.1. CO-*emitting Regions*

As seen in the moment map presented in Figure 2, there are three regions where we have detected CO emission in NGC 4214—one at the center of the galaxy, another ∼650 pc to the southeast of the center, and the third ∼760 pc to the northwest. The southeastern region has the highest peak in CO emission and is also the most centrally concentrated. The central region is extended in the east-west direction, with low-intensity CO emission that has a diffuse appearance except for the concentration at its western end. The northwestern region is intermediate between the central and the southeastern ones, both in the degree of central concentration and the intensity of the emission.

Each of the regions can be divided into discrete units (clumps) by considering both the spatial and velocity information given in the data cube. To do that, we inspected the high-resolution, robust-weighted cubes by looking at "movies," as well as position-velocity (PV) diagrams. The clump decomposition is difficult in the northwestern and southwestern regions, where many smaller units are blended. Figure 4 shows a PV diagram of the northwestern region as an example of how we defined the clumps (the ellipses plotted in this figure are only used to label the clumps). The properties of the identified CO-emitting clumps in NGC 4214 are compiled in Table 4. C1–C8 belong to the northwestern complex, C9 belongs to the

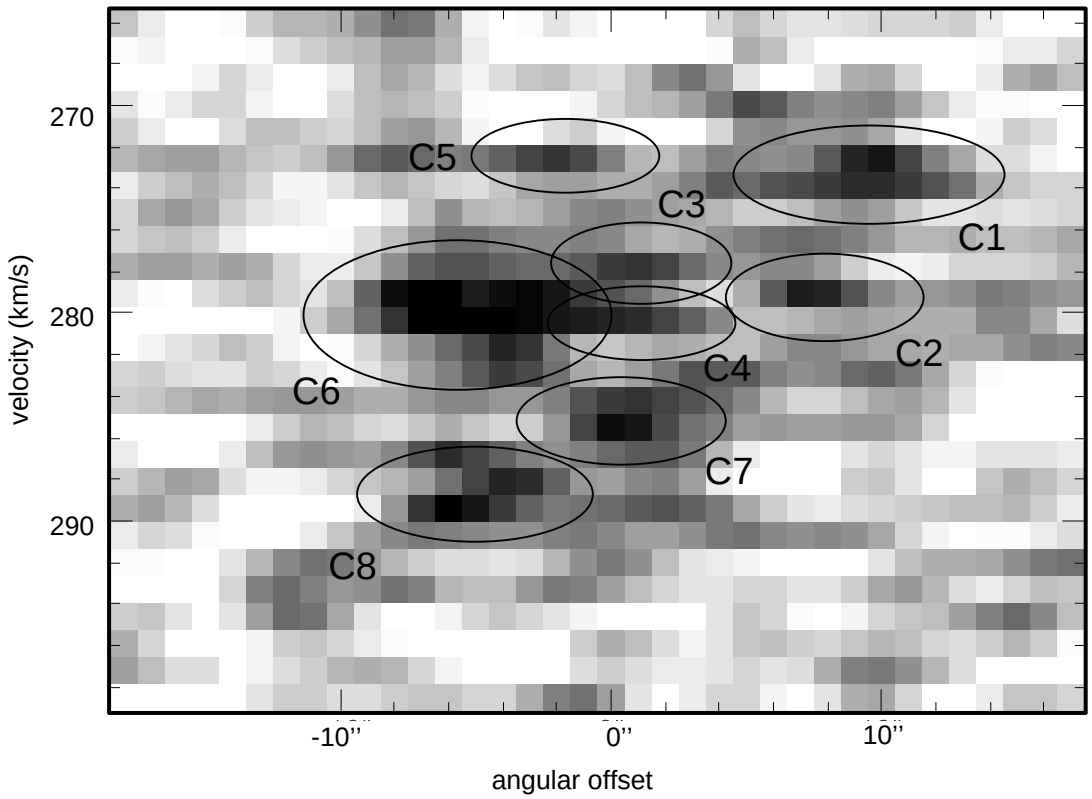

FIG. 4.—PV diagram indicating the subdivisions of the CO emission in the northwestern complex (*ellipses*). The numbers refer to the clumps as listed in Table 4. The PV cut is centered at R.A. = 12^{h}15^{m}36^s.5, decl. = 36°20′02″ (J2000.0), and the position angle is 270° (east-west).

TABLE 4

PROPERTIES OF CO-EMITTING REGIONS

Cloud (1)	α (J2000.0) (2)	δ (J2000.0) (3)	v_{cen}[a] (km s^{-1}) (4)	Δv_{FWHM} (km s^{-1}) (5)	S_{CO} (Jy km s^{-1}) (6)	D_{dec}[b] (pc) (7)	M_X[c] ($10^5\ M_\odot$) (8)	M_{vir}[d] ($10^5\ M_\odot$) (9)
C1.....	12 15 35.2	36 19 59	272	3.5	1.16	100	2.4	1.5
C2.....	12 15 35.9	36 20 01	279	2	0.35	[e]	0.7	(0.4)[f]
C3.....	12 15 36.5	36 20 02	278	1.5	0.23	[e]	0.5	(0.2)
C4.....	12 15 36.4	36 20 02	280	1.5	0.27	[e]	0.6	(0.2)
C5.....	12 15 36.7	36 20 03	272	4	0.28	[e]	0.6	(1.7)
C6.....	12 15 36.9	36 20 02	280	6.5	1.56	100	3.2	5.1
C7.....	12 15 36.6	36 20 02	285	4.5	0.87	[e]	1.8	(2.2)
C8.....	12 15 37.0	36 20 03	288	3	1.31	100	2.7	1.1
C1–C8	...	...	...	...	6.03	...	12.5	...
C9.....	12 15 38.3	36 19 33	298	10	2.9	[e]	6	(10.8)
D1	12 15 39.7	36 19 31	...	...	4.0	...	8.3	...
D1+C9.....	...	...	...	...	6.9	...	14.3	...
C10	12 15 41.0	36 19 10	296	6	1.25	[e]	2.6	(3.9)
C11	12 15 41.0	36 19 5	287	6	1.02	80	2.1	3.4
C12	12 15 40.8	36 19 2	301	9	7.17	100	14.8	9.7
C13	12 15 41.7	36 19 3	296	3.5	0.57	[e]	1.2	(1.3)
C14	12 15 41.7	36 19 12	128	6	1.53	[e]	3.2	(3.9)
C10–C14.....	...	...	...	...	11.54	...	23.9	...
Sum	...	...	...	...	...	...	50.7	...

NOTE.—Units of right ascension are hours, minutes, and seconds, and units of declination are degrees, arcminutes, and arcseconds.

[a] Velocities are v_{LSR} ($v_{hel} = v_{LSR} - 6.5$ km s^{-1}).

[b] Diameters are deconvolved for beam size (4.″8 × 4.″2).

[c] Molecular masses are derived using $M_X = (1.23 \times 10^4)4.1^2 S_{CO}\ M_\odot$. This assumes a "standard" CO-to-H_2 conversion factor of 2.3×10^{20} cm^{-2} (K km s^{-1})$^{-1}$ (Strong et al. 1988) and includes an additional factor of 1.36 as a correction for helium. If the recalibrated conversion factor of $X = 1.6 \times 10^{20}$ cm^{-2} (K km s^{-1})$^{-1}$ (Hunter et al. 1997) is used, all CO-based masses have to be reduced by ~30%.

[d] Virial masses are derived, using $M_{vir} = 240 v^2_{FWHM}(D/2)$, where v is in km s^{-1} and D is in pc.

[e] Not resolved with the 4.″8 × 4.″2 (~90 pc) beam.

[f] Numbers in parentheses are virial masses derived for a cloud diameter of 90 pc (see § 4.1).

central complex, where some diffuse emission is also present (D1), and C10–C14 are the constituents of the southeastern emission feature in NGC 4214.

For each clump, we derived a total intensity map and measured the diameter defined by the half-intensity line and the velocity width: Table 4 lists the central coordinates (cols. [2] and [3]), the central velocity of the clump (col. [4]), the velocity width (FWHM, col. [5]), and the CO flux (col. [6]), as well as the diameter of the clump (FWHM, col. [7]) along the cut deconvolved for our beam size (average of the orthogonal directions). In many cases, only an upper limit for the cloud size could be determined (as given by the size of the robust beam). We also attempted to estimate molecular masses by employing a Galactic X-factor (col. [8]; see § 4.1) and assuming virialization (col. [9]; but see the discussion in § 4.1).

C1–C14 are likely not giant molecular clouds (GMCs). This can be seen in Figure 5, where we show the size–to–line width relation for GMCs in M33 from Wilson & Scoville (1990), along with GMCs from M33, M31 (Vogel, Boulanger, & Ball 1987; Wilson & Rudolph 1993), the Small Magellanic Cloud (Rubio, Lequeux, & Boulanger 1993), IC 10 (Wilson 1995), NGC 1569 (Taylor et al. 1999) and NGC 6822 (Wilson 1994), and our complexes. The three complexes resolved by the OVRO beam clearly occupy a different region in the plot than GMCs in Local Group galaxies. They have similar line widths but are larger in size. The unresolved clouds may be individual GMCs, but their diameters are too small to measure with the synthesized beam of our data.

The clumps we see fall in an area in the size–to–line width space that is in between the Local Group galaxies and CO complexes in M83 (Rand, Lord, & Higdon 1999), also plotted in Figure 5. Rand et al. argue that their objects are intermediate in size, line width, and molecular mass between the largest GMCs known in the Milky Way and giant molecular associations (GMAs) seen in nearby spiral galaxies (e.g., Rand & Kulkarni 1990). Our resolved objects

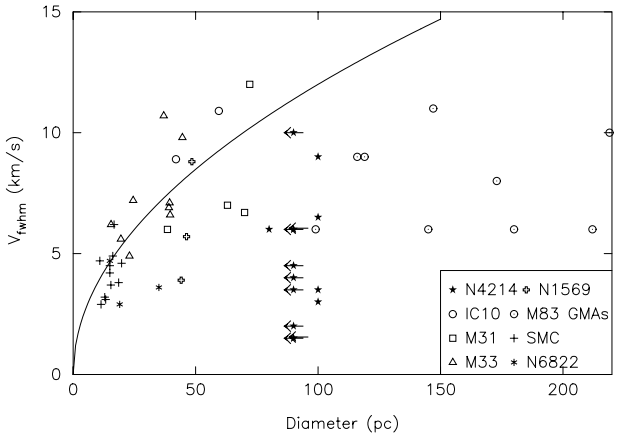

FIG. 5.—Diameter–to–line width relationship for GMCs in Local Group galaxies. The clouds in different galaxies are plotted as different symbols, and the line shows a best-fit relationship to the M33 GMCs derived by Wilson & Scoville (1990). Upper limits are given for the spatially unresolved objects in NGC 4214.

have smaller diameters compared with the Rand et al. objects—they are probably not GMAs. Also, GMAs tend to have masses of a few times $10^7\ M_\odot$, whereas for an assumed Galactic CO-to-H_2 conversion factor, our clumps have masses that are lower by almost 2 orders of magnitude.

3.2. *Comparison with the* H I

Starbursting dwarf galaxies tend to be H I–rich (see, e.g., Thuan & Martin 1981; Taylor et al. 1995), and NGC 4214 is no exception. Figure 6 shows the CO contours from Figure 2 superposed on the total intensity map of the H I emission (corrected for primary-beam attenuation). The high-resolution H I data are combined with B-, C-, and D-configuration observations from the VLA, with a spatial resolution of $8'' \times 8''$ (see also McIntyre 1998). The area we have mapped in CO covers only a small region at the center of NGC 4214. The peak column density of H I in the map is $\sim 3 \times 10^{21}$ cm^{-2}, and the overall H I distribution shows a large degree of structure: H I holes and shells, which are common in dwarf galaxies (see, e.g., Puche et al. 1992; Walter & Brinks 1999). There is also some indication for spiral structure extending beyond the main optical disk. There is even a hint of a bar in the H I, running roughly through the center of the galaxy at a position angle of 45° (north to west). It is possible that both the weak spiral features and the bar are consequences of an interaction with the nearby dwarf galaxy NGC 4190. There are a few dwarf galaxies, such as Holmberg II (Puche at al. 1992) and DDO 47 (Walter & Brinks 2001), that show similar spiral features in H I only. The underlying process that causes transient spiral structure may thus be fairly common.

A global comparison between the H I and CO emission reveals differences between the various CO-emitting regions. The northwestern region of CO emission falls on top of a local maximum in the H I column density, while the southeastern region, which is brighter and more centrally concentrated, corresponds to a dip in the H I column density near two local peaks. The central CO region is extended enough to cover several local minima and maxima in the H I, though the shape of the H I is elongated east-west, similar to the CO emission. It should be noted here that the strongest molecular emission is not necessarily found where the H I column densities are highest. This finding emphasizes the "irregular" nature of dIrr's.

The CO and H I channel maps are compared in Figure 1. This representation of the data emphasizes more strongly the location of the southeastern CO emission in a small H I dip and the association of the northwestern CO emission region with a local H I maximum roughly coincident in velocity. There is no clear correlation in the channel maps between CO and H I for the central CO feature. Figure 7 is a PV diagram through the three brightest CO peaks and compares the CO and H I velocities and intensities in and near these peaks. For the southeastern (offset: $-0\farcs75$) and central peaks, the CO line widths are much narrower than the corresponding H I line widths. In contrast, in the northwestern peak (at offset $0\farcs7$), the CO line width is larger, probably because of substructure in the complex, and approaches the velocity width of the H I to within a factor of ~ 1.5.

3.3. *Comparison with Stellar Component and Regions of Star Formation*

Star formation occurs at densities where the gas is primarily molecular, so it is of interest to compare the molecular gas tracer, CO, with tracers of the stellar component. Because the ISM is readily ionized by the intense UV radiation from young stars in H II regions, Hα is often used as an indicator of the presence of recent star formation. Figure 3 compares the CO emission with an Hα image (courtesy of C. Martin). The left panel shows lacy, filamentary structures outside the immediate vicinity of the star-forming regions. These are similar to those seen in other dwarf galaxies (e.g., NGC 1569; Hunter, Hawley, & Gallagher 1993; Devost,

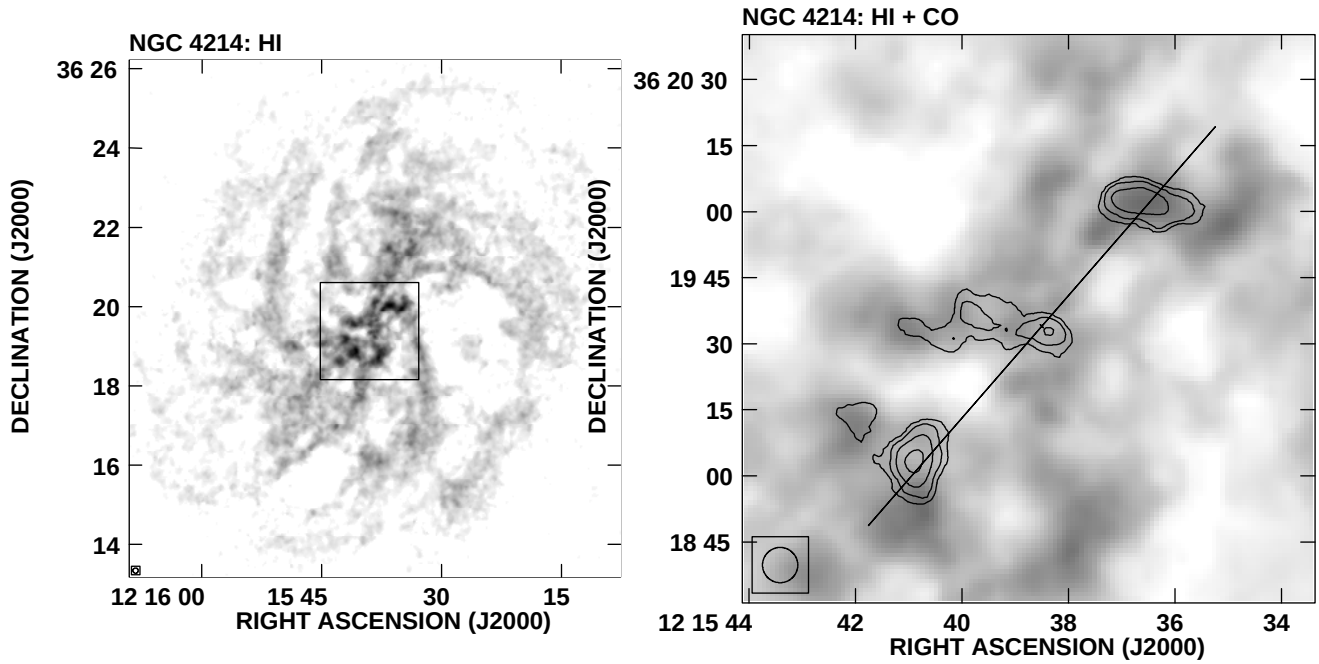

FIG. 6.—*Left:* Integrated intensity of H I in NGC 4214. The center box indicates the region shown in the right panel. *Right:* Naturally weighted CO contours from Fig. 2 superposed on the H I integrated intensity map. The line indicates the orientation of the PV cut presented in Fig. 7 (*right*).

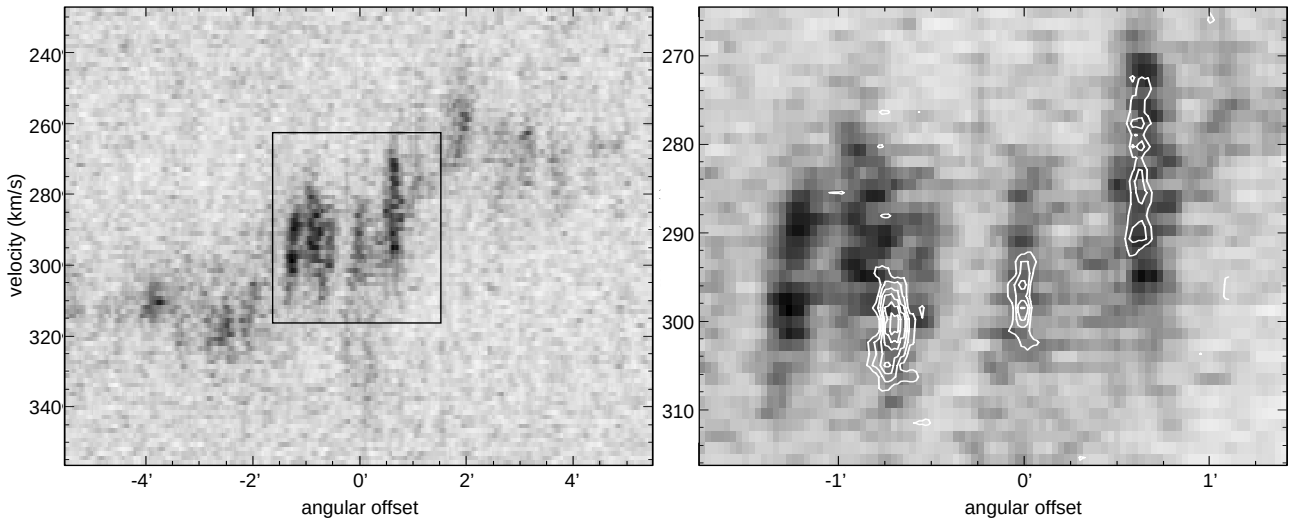

FIG. 7.—*Left:* PV diagram of the H I distribution (center: R.A. = $12^h15^m38^s.5$, decl. = 36°19′34″ [J2000.0], position angle: 319°). The center box indicates the region shown in the right panel. *Right:* H I PV diagram with CO contours (*white*) superposed (see the line in Fig. 6, *left*, for the orientation of this cut).

Roy, & Drissen 1997; Martin 1998) and are presumably caused by the energetic by-products of star formation, supernovae, and stellar winds.

Two of the three CO complexes are associated directly with the star-forming regions (Fig. 3, *right*). The southeastern CO clump appears cospatial, with a large star-forming complex containing several H II regions. The peak of the CO emission here is almost directly on top of one of the H II regions, and the shape of the CO complex, with its slight extension in the north-south direction, is very similar to that of the H II region. The central CO emission is associated with the largest region of Hα emission. Unlike the southeastern complex, the central CO complex is diffuse instead of centrally concentrated, and the peak of the CO emission here is not directly on top of the Hα emission but is shifted to the west of it. Lower level CO emission is cospatial with the Hα emission, however, tracing out the chain of brighter H II regions running east-west in this area. In clear contrast, only very faint Hα emission is associated with the northwestern CO complex.

At this point it is interesting to compare the velocities of the molecular gas with the ones of the ionized component (as seen in Hα spectra). Hartmann, Geller, & Huchra (1986) presented the kinematics of a few H II regions within NGC 4214—four of them correspond to regions where we also detected CO emission (their regions H25/29, close to our northwestern CO complex; H36 and H48, toward the central complex; and H55 in the southeastern complex). In all cases, the systemic CO and Hα velocities do agree well (this is consistent with the results by Maíz-Apellániz et al. 1999). Only in H25/29 (the weakest of the four Hα regions) is Hα emission also present at velocities where no CO emission is present (around $v_{\rm hel} = 250$–270 km s^{-1}).

Figure 8 shows the contours of the CO emission superposed on a multiband optical image created by the Hubble Heritage Team. Here the quite different optical morphologies of the regions where CO emission is found are evident more dramatically. This composite image was created from different Wide Field Planetary Camera 2 pointings in the F336W (*U*), F502N ([O III]), F555W (*V*), F656N (Hα), F702N (*R*), and F814W (*I*) filters. A detailed discussion of these data has been published by MacKenty et al. (2000).

Both Beck, Turner, & Kovo (2000) and MacKenty et al. (2000) present high-resolution VLA radio continuum images. There are 6 and 20 cm emissions associated with the central and southeastern star-forming complexes, but nothing is detected at the location of the northwestern CO emission (J. Turner 2000, private communication). This lack of radio continuum emission indicates that, indeed, very little star formation is associated with the northwestern molecular region (C1–C8), and that the presence of only very weak optical emission lines is not due to possible extinction.

4. DISCUSSION

4.1. CO-*to*-H_2 *Conversion Factor*

To determine the conversion factor with a reasonable degree of confidence, a discrete unit of emission, such as a GMC, must be distinguishable in the data, and there must be a method to determine the total mass associated with this feature, which is independent of CO intensity. GMCs are often assumed to be gravitationally bound and in virial equilibrium, allowing the use of the virial theorem to determine the total mass. As discussed above, our spatial resolution will not resolve GMC-sized objects at the distance of NGC 4214. For the sake of comparison, we decided to derive virial masses for our clumps anyway—in the discussion that follows, we will keep in mind that at least some of them are likely *not* gravitationally bound objects. In the cases where the complex is not spatially resolved, we take the beam size ($D \sim 90$ pc) as an upper limit for the actual diameter—then, the virial masses are probably upper limits (but see the discussion below). If the virial mass could be trusted, dividing it by the molecular mass derived using a Galactic CO-H_2 conversion factor would yield the actual conversion factor for each feature in units of the Galactic value. The Galactic conversion factor is taken to be 2.3×10^{20} cm^{-2} (K km s^{-1})$^{-1}$ (Strong et al. 1988), with an additional explicit correction for helium (see Table 4, note c). If the recalibrated conversion factor of 1.6×10^{20} cm^{-2} (K km s^{-1})$^{-1}$ (Hunter et al. 1997) or the new value advocated by Dame et al. 2001 (1.8×10^{20} cm^{-2} [K km s^{-1}]$^{-1}$) is used, all CO-based masses are lower by $\sim$30%. To facili-

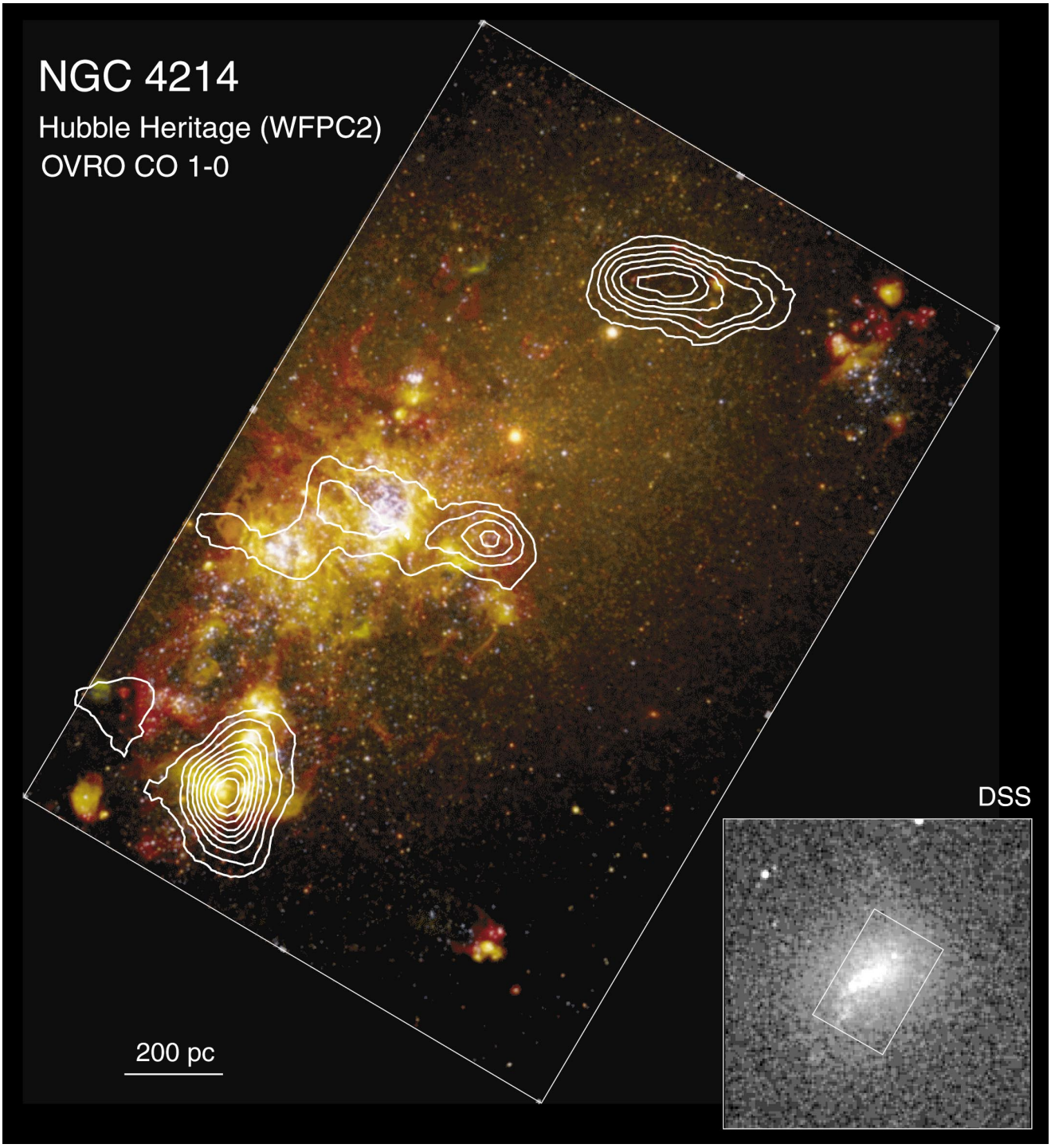

FIG. 8.—Naturally weighted CO contours from Fig. 2 superposed on a multiwavelength F336W (*U*), F502N ([O III]), F555W (*V*), F656N (Hα), F702N (*R*), and F814W (*I*) image created by the Hubble Heritage Team from WFPC2 data.

tate comparison with previous work, the numbers we give refer to the "standard" value of Strong et al.

The average conversion factor we find for the few resolved features is compatible with the standard Galactic conversion factor (Table 4) given all the uncertainties in deriving these numbers. The mean conversion factor is $\sim (1.2 \pm 0.7) X_{\rm MW}$, whether or not only the resolved clouds or all clouds are used for the estimate. This is a lower value than the conversion factor estimated for other dwarf galaxies with similar metallicities in the literature ($2.7 X_{\rm MW}$ for the dIrr IC 10, less than $2.2 X_{\rm MW}$ for the dIrr NGC 6822, both in the Local Group [Wilson 1995], and $6.6 X_{\rm MW}$ in the poststarburst dwarf galaxy NGC 1569 [Taylor et al. 1999]).

This result is unexpected at first glance, since one would expect the *X*-factor to be higher in this low-metallicity galaxy (as suggested by other studies of low-metallicity dwarfs; see above). We can only speculate here why the results in NGC 4214 are different. We would like to note that the virial masses are strongly affected and possibly even dominated by the resolution (both spatially and

kinematically) employed in the observations. For example, if we use our naturally weighted, 5 km s^{-1} channel width data (i.e., if we do not resolve the substructure) we derive a virial mass for the northwestern complex that is several times larger than the mass derived using X_{MW}. This is because of the fact that the dispersion in the northwestern region is rather large ($\Delta v \sim 20$ km s^{-1}), resulting in a much higher X-factor (because of the Δv^2 dependence of the virial mass)—in other words, our result would then be consistent with the values found in other low-metallicity galaxies! It should also be stressed here that deriving cloud properties (and hence virial masses) is not at all an objective process: for example, different radii have been used by different authors (e.g., diameter defined by the half-intensity line or by the contour containing 90% of the flux), and the cloud sizes are not always deconvolved for the beam size. Dividing clumps into subclumps is also always subject to some personal bias.

It should be also noted at this point that convincing arguments have been presented (see, e.g., Bolatto, Jackson, & Ingalls 1999; Madden et al. 1997) for a cloud structure in dwarf galaxies that significantly differs from what is found in metal-rich giant spirals. In this scenario, small CO cores are embedded in huge molecular envelopes that are devoid of CO. The molecular hydrogen in the envelopes coexists with C I and C II. For example, Madden et al. argue that in the dwarf irregular IC 10 the total molecular mass may be up to 100 times the mass contained in the CO cores. In this case, our CO observations would only trace the cores of the clouds and the derived "local" X-factor would be only valid for the central core of a molecular cloud, where it might indeed be close to the Galactic value, since the conditions in the core region are expected to be similar to those in a Galactic GMC.

Unfortunately, based on the data presented here, all this remains subject to speculation. In the case of NGC 4214, the matter might be investigated further by a comprehensive study of the CO, C I, C II, radio continuum, and far-IR emissions, along the lines of the study Madden et al. performed for the (much closer) galaxy IC 10.

Based on our data, we will adopt X_{MW} as the conversion factor for NGC 4214 in the following, primarily for convenience. We keep in mind that this number is unfortunately only poorly determined and that our estimated molecular gas mass might be off by a factor of 2–3.

4.2. *Star Formation Efficiency*

Given the fact that the southeastern molecular cloud seems not yet to be disrupted by the ongoing burst of star formation (see the discussion in § 4.4), we can try to calculate the star formation efficiency for that region. From Table 3 of MacKenty et al. (2000), we derive a star formation rate (SFR) for this region of 0.066 $M_\odot$ yr^{-1} (their region II, corrected for "medium internal extinction"). For morphological reasons (e.g., the compact and filled appearance of the H II regions, the lack of large cavities, and the positional coincidence of exciting star clusters and Hα-emitting knots), star formation presumably only recently started here—we adopted an age of ~ 3 Myr (MacKenty et al. 2000). This results in a total stellar mass of $\sim 2.0 \times 10^5$ $M_\odot$ produced to date (assuming a constant SFR). From our Table 4, we derive a molecular mass of 24×10^5 $M_\odot$ (summing up regions C10–C14 and adopting a Galactic X-factor; see the discussion in § 4.1). The star formation efficiency for the southeastern region is thus around 8%, somewhat higher than what is usually adopted (see also, e.g., Wilson & Matthews 1995 and the discussion in Taylor et al. 1999).

4.3. *Star Formation Threshold*

Studies of star-forming dwarf galaxies suggest that the gas column density plays an important role in regulating star formation (Skillman et al. 1987; Taylor et al. 1994; Walter et al. 1997; van Zee, Skillman, & Salzer 1998; Walter & Brinks 1999). A threshold column density for the onset of star formation is thought to exist, at $\sim 10^{21}$ cm^{-2}, above which massive star formation can proceed and below which it is suppressed. The physical reason for this threshold may be related to the density needed for the shielding of molecular gas from dissociating radiation (see, e.g., Skillman 1987), or perhaps to disk instabilities (see, e.g., Kennicutt 1989). For this kind of analysis, generally some measure of the spatial extent of the star formation activity (such as an Hα image) is compared with the azimuthally averaged gas surface density (usually based on H I observations) or with the contours of an H I column density map. Because CO is difficult to detect in most dwarf galaxies, the previous studies have tended to ignore the presence of molecular gas entirely or else have attempted to make a statistical correction by assuming a global H_2–to–H I ratio (Hunter & Plummer 1996). However, we have high-resolution CO and H I data on NGC 4214, covering the star-forming regions of the galaxy, so we can treat *both* the atomic and the molecular gas in the threshold analysis.

We created a total gas column density map by combining the H I and CO moment maps and using a Galactic CO-H_2 conversion factor (see § 4.1). Figure 9 shows the contours for column densities of 1, 2, and 4×10^{21} cm^{-2} (corrected for an inclination of 30°; McIntyre 1997) for the total gas map and the H I map alone, superposed on the Hα image from Figure 3. There is hardly any change in the lowest contour, indicating that at densities of 10^{21} cm^{-2} the gas is primarily in atomic form. The higher contours, however, show marked changes from H I alone to total gas density, particularly at the location of the southeastern CO complex. In the total gas map, we see a peak in gas density corresponding to the group of H II regions, whereas if we consider the H I alone, the Hα emission sits in a local minimum of density adjacent to two local peaks. The peak gas density in the total gas map at this complex is 6.6×10^{21} cm^{-2}. In the central complex, the addition of the molecular component also makes a difference, connecting two H I peaks that straddle the center of the star-forming complex.

From Figure 9, it is apparent that there is only very faint Hα emission associated with the CO emission of the northwestern complex, suggesting very little star formation. This lack of activity is confirmed by the nondetection of radio continuum emission at the position of the northwestern complex. The peak (H I + H_2) column density here is 95% of that of the southeastern clump, where we see evidence for vigorous star formation. The column density in the central, very active star-forming region is considerably lower, but this could be explained by the influence of the massive stars upon the ISM in a more evolved star formation region (see the next section). A plausible explanation for the lack of star formation in the northwestern complex is suggested by the comparison of the CO and H I velocities and/or line widths in Figure 7. Here we see that the line width in CO in the

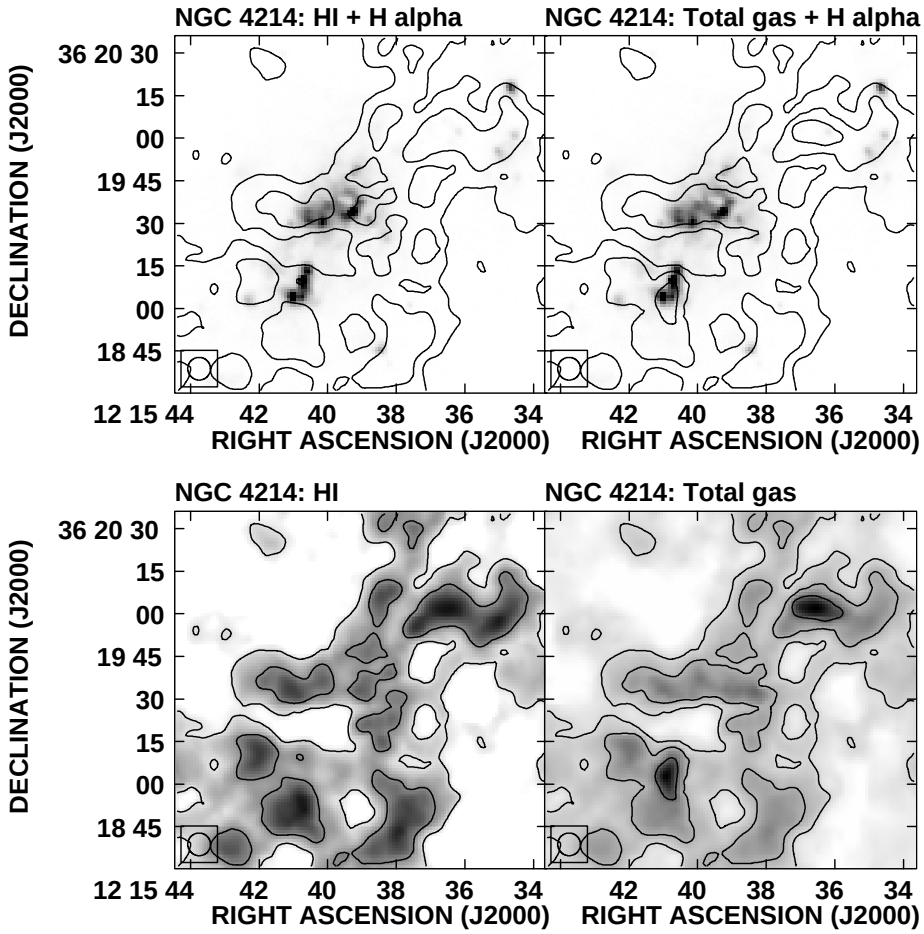

FIG. 9.—*Top left:* H I column density corrected for inclination, with contour levels at 1 and 2 × 10^{21} cm^{-2}. *Top right:* Total gas (H I + H_2) column density corrected for inclination, with contour levels of 1, 2, and 4 × 10^{21} cm^{-2}. To facilitate the interpretation of the contours in the top two panels, gray-scale plots are presented at the bottom.

northwestern complex is comparable with the H I line width, while for the other two complexes CO is much narrower. Perhaps the *surface* density along the line of sight to the northwestern complex is high, but the *volume* density is not. The large line width and identifiable substructure in the northwestern complex suggests a distribution of clouds at different velocities along the line of sight, rather than one dense cloud. It may also be that star formation has simply not started yet in the northwestern complex, in which case another episode of star formation might begin in the near future.

4.4. *Effects of the Star Formation Burst on the ISM*

Massive stars, the most prominent constituents of star-forming regions, input energy into the ISM through mechanisms, such as ionizing photons, stellar winds, and supernovae, and it is inevitable that they will disrupt the local ISM. In some dwarf galaxies, such as IC 2574, swept-out holes in the H I accumulate large quantities of gas on their rims, providing material for a second generation of star formation (Walter et al. 1998; Stewart & Walter 2000). In NGC 4214, there is no evidence for this. There are certainly a number of holes in the H I (Fig. 6), but the star-forming regions do not appear along their rims (as is apparent in the supergiant shell in IC 2574). There are several small expanding shells of ionized gas associated with the central star-forming region (Martin 1998), and these might later develop H I shells like those seen in IC 2574.

On scales of a few hundred parsecs, the ISM shows indications of the effects of the massive stars. The H II regions in the central star-forming complex show a shell morphology (Figs. 8 and 9), which suggests that these shells have broken through the dense material surrounding the massive stars. The southeastern H II regions still show compact, knotlike morphologies, suggesting that a breakout has not yet occurred (MacKenty et al. 2000). If the starburst of the central region preceded the southeastern one, then the massive stars in the center have been at work dissociating and disrupting the molecular gas for longer than in the southeastern. Thus the CO intensity associated with the shell H II regions is lower, and the emission is more diffuse than ~200 pc to the west, where the highest CO intensity in the central complex is found, away from the immediate vicinity of any H II region. The brightest CO emission in the galaxy, associated with the H II regions in the southeastern complex, may represent a predisruption stage, where the energy input into the ISM from the young stars has not had enough time to affect a large fraction of the molecular gas or the general morphology of the complex and is thus not visible in our 90 pc resolution observations. In summary,

NGC 4214 seems to show molecular gas and star formation in three distinct stages: high-dispersion molecular gas with hardly any associated star formation in the northwest, concentrated molecular gas with very recent star formation in the southeast, and diffuse molecular gas with an older massive star formation burst in the center.

5. SUMMARY AND CONCLUSIONS

We have mapped the dwarf starburst galaxy NGC 4214 in the ^{12}CO (1–0) transition at the OVRO millimeter array with a linear resolution of $\sim$90 pc. This first high-resolution study of the molecular component in this galaxy shows the presence of three molecular complexes that are in very different and distinct evolutionary stages. Both from the properties of the molecular gas and from the *HST* and ground-based optical studies of the H II regions and star clusters, the central region is the most evolved: Here the molecular complex is highly disrupted, the impact of the massive star formation is largest, and a shell structure is in the process of forming. The star formation episode in the southeastern complex is more recent; thus, the dense ISM adjacent to the newly formed massive stars is far less disrupted, providing an ideal environment for ongoing, maybe self-propagating, star formation proceeding further into the complex. Somewhat surprisingly, massive star formation has not started yet in the northwestern complex, possibly because the threshold volume density has not been reached in this region.

A comparison with the H I reveals that no clear correlation between the H I and CO surface densities exists. Although the northeastern and southwestern regions have almost the same total (H I and H_2) gas column density, violent star formation is only taking place in the southwestern region. This nicely illustrates the irregular nature of these dwarf systems. The H I and Hα velocities are in good agreement with the CO velocities measured in the three molecular complexes. Assuming a Galactic conversion factor, the star formation efficiency for the southeastern complex is $\sim$8%, similar to that found for spiral galaxies. This may be taken as an indication that the star formation process itself in dwarf galaxies proceeds in a way similar to that in spirals.

We were able to subdivide the molecular complexes further into 14 subcomplexes. Most of the clumps cannot be resolved with our synthesized beam—even the resolved objects are probably not GMCs. Deriving virial masses from these objects is not trivial and is affected by personal bias and the employed velocity and spatial resolution. Our clump analysis is compatible with a Galactic conversion factor for NGC 4214; this is substantially lower than the value found so far in other dwarf galaxies with similar metallicities. However, given the uncertainties in deriving this value we cannot rule out the validity of the metallicity-X relation based on our data. We derive a total molecular mass for NGC 4214 of $5.1 \times 10^6\ M_\odot$.

In summary, our OVRO observations of the molecular gas in the metal-poor dwarf galaxy NGC 4214 reveal an unexpected structural wealth—they serve as a good excuse to map similar low-metallicity dwarf galaxies with interferometers in the future: even though the emission is faint when compared with spiral galaxies, high-resolution observations of the molecular gas can provide important insights to the irregular nature of dwarf galaxies.

We thank C. Martin for providing us with her Hα image of NGC 4214. F. W. acknowledges National Sciene Foundation grant AST 96-13717. V. M. was supported in part by a Smithsonian Predoctoral Fellowship and an Australian Postgraduate Research Award. Support of this work was also provided by a grant from the K. T. and E. L. Norris Foundation. Research with the Owens Valley Radio Telescope, operated by California Institute of Technology, is supported by NSF grant AST 96-13717. The Five College Radio Astronomy Observatory is operated with the permission of the Metropolitan District Commission, Commonwealth of Massachusetts, and with the support of the NSF under grant AST 97-25951. The National Radio Astronomy Observatory is operated by the Association of Universities for Research in Astronomy (AURA), Inc., under cooperative agreement with the NSF. The home of the Hubble Heritage Project is the Space Telescope Science Institute, which is operated by AURA, Inc., for NASA. This research has made use of the NASA/IPAC Extragalactic Database, which is operated by the Jet Propulsion Laboratory, California Institute of Technology, under contract with NASA. The authors also acknowledge the use of NASA's Astrophysical Data System Abstract Service and SkyView.

REFERENCES

Allsopp, N. J. 1979, MNRAS, 188, 765
Arimoto, N., Sofue, Y., & Tsojimoto T. 1996, PASJ, 48, 275
Barone, L. T., Heithausen, A., Hüttemeister, S., Fritz, T., & Klein, U. 2000, MNRAS, 317, 649
Beck, S. C., Turner, J. L., & Kovo, O. 2000, AJ, 120, 244
Becker, R., Henkel, C., Bomans, D. J., & Wilson, T. L. 1995, A&A, 295, 302
Bolatto, A. D., Jackson J. M., & Ingalls, J. G. 1999, ApJ, 513, 275
Briggs, D. S. 1995, Ph.D. thesis, New Mexico Inst. Mining Technol.
Dame, T. M., Hartmann, D., & Thaddeus, P. 2001, ApJ, in press
de Vaucouleurs, G., de Vaucouleurs, A., Corwin, H. G., Jr., Buta, R. J., Paturel, G., & Fouqué, P. 1991, Third Reference Catalogue of Bright Galaxies (New York: Springer)
Devost, D., Roy, J.-R., & Drissen, L. 1997, ApJ, 482, 765
Hartmann, L. W., Geller, M. J., & Huchra, J. P. 1986, AJ, 92, 1278
Huchra, J. P., Geller, M. J., Gallagher, J., Hunter, D., Hartmann, L., Fabbiano, G., & Aaronson, M. 1983, ApJ, 274, 125
Hunter, D. A., Hawley, W. N., & Gallagher, J. S. 1993, AJ, 106, 1797
Hunter, D. A., & Plummer, J. D. 1996, ApJ, 462, 732
Hunter, S. D., et al. 1997, ApJ, 481, 205
Kennicutt, R. C. 1989, ApJ, 344, 685
Kobulnicky, H. A., & Skillman, E. D. 1996, ApJ, 471, 211
Leitherer, C., Vacca, W. D., Conti, P. S., Filippenko, A. V., Robert, C., & Sargent, W. L. W. 1996, ApJ, 465, 717
Li, J. G., Seaquist, E. R., Wang, Z., & Sage, L. J. 1994, AJ, 107, 90
MacKenty, J. W., Maíz-Apellániz, J., Piccens, C. E., Norman, C. A., & Walborn, N. R. 2000, AJ, 120, 3007
Madden, S. C., Poglitsch, A., Geis, N., Stacey, G. J., & Towney, C. H. 1997, ApJ, 483, 200
Maíz-Apellániz, J., Muñoz-Tuñón, C., Tenorio-Togle, G., & Mas-Hesse, J. M. 1999, A&A, 343, 64
Maloney, P., & Black, J. H. 1988, ApJ, 325, 389
Martin, C. L. 1998, ApJ, 506, 222
McIntyre, V. J. 1997, Publ. Astron. Soc. Australia, 14, 122
———. 1998, Publ. Astron. Soc. Australia, 15, 157
Norman, C. A., & Spaans, M. 1997, ApJ, 480, 145
Ohta, K., Tomita, A., Saito, M., Sasaki, M., & Nakai, N. 1993, PASJ, 45, L21
Puche, D., Westpfahl, D. Brinks, E., & Roy, J.-R. 1992, AJ, 103, 1841
Rand, R. J., & Kulkarni, S. R. 1990, ApJ, 349, L43
Rand, R. J., Lord, S. J., & Higdon, J. L. 1999, ApJ, 513, 720
Rubio, M., Garay, G., Montani, J., & Thaddeus, P. 1991, ApJ, 368, 173
Rubio, M., Lequeux, J., & Boulanger, F. 1993, A&A, 271, 9
Shen, J., & Lo, K. Y. 1995, ApJ, 445, L99
Skillman, E. D. 1987, in Star Formation in Galaxies, ed. C. Persson (Washington: NASA), 263
Skillman, E. D., Bothun, G. D., Murray, M. A., & Warmels, R. H. 1987, A&A, 185, 61

Stewart, S. G., & Walter, F. 2000, AJ, 120, 1794
Strong, A. W., et al. 1988, A&A, 207, 1
Swaters, R. 1999, Ph.D. thesis, Univ. Croningen
Tacconi, L. J., & Young, J. S. 1985, ApJ, 290, 602
Taylor, C. L., Brinks, E., Grashuis, R. M., & Skillman, E. D. 1995, ApJS, 99, 427 (erratum 102, 189 [1996])
Taylor, C. L., Brinks, E., Pogge, R. W., & Skillman, E. D. 1994, AJ, 107, 971
Taylor, C. L., Hüttemeister, S., Klein, U., & Greve, A. 1999, A&A, 349, 424
Taylor, C. L., Kobulnicky, H. A., & Skillman, E. D. 1998, AJ, 116, 2746
Thronson, H. A., Hunter, D. A., Telesco, C. M., Greenhouse, M., & Harper, D. A. 1988, ApJ, 334, 605
Thuan, T. X., & Martin, G. E. 1981, ApJ, 247, 823
Turner, J. L., Beck, S. C., & Hurt, R. L. 1997, ApJ, 474, L11
van Zee, L., Skillman, E. D., & Salzer, J. J. 1998, AJ, 116, 1186
Verter, F., & Hodge, P. 1995, ApJ, 446, 616
Vogel, S. N., Boulanger, F., & Ball, R. 1987, ApJ, 321, L145
Walter, F., & Brinks, E. 1999, AJ, 118, 273
———. 2001, AJ, submitted
Walter, F., Brinks, E., Duric, N., & Klein, U. 1997, AJ, 113, 2031
Walter, F., Kerp, J., Duric, N., Brinks, E., & Klein, U. 1998, ApJ, 502, L143
Walter, F., Weiss, A., Martin, C., & Scoville, N. 2001, AJ, in preparation
Wilson, C. D. 1994, ApJ, 434, L11
———. 1995, ApJ, 448, L97
Wilson, C. D., & Matthews, B. C. 1995, ApJ, 455, 125
Wilson, C. D., & Reid, I. N. 1991, ApJ, 366, L11
Wilson, C. D., & Rudolph, A. L. 1993, ApJ, 406, 477
Wilson, C. D., & Scoville, N. 1990, ApJ, 363, 435
Young, L. M., & Lo, K. Y. 1997, ApJ, 476, 127